Article

Kinetic analysis of receptor-activated phosphoinositide turnover

Chang Xu, James Watras, and Leslie M. Loew

Department of Physiology and Center for Biomedical Imaging Technology, University of Connecticut Health Center, Farmington, CT 06030

We studied the bradykinin-induced changes in phosphoinositide composition of N1E-115 neuroblastoma cells using a combination of biochemistry, microscope imaging, and mathematical modeling. Phosphatidylinositol-4,5-bisphosphate (PIP_2) decreased over the first 30 s, and then recovered over the following 2–3 min. However, the rate and amount of inositol-1,4,5-trisphosphate ($InsP_3$) production were much greater than the rate or amount of PIP_2 decline. A mathematical model of phosphoinositide turnover based on this data predicted that PIP_2 synthesis is also stimulated by bradykinin, causing an early transient increase in its concentration. This was subsequently confirmed experimentally. Then, we used single-cell microscopy to further examine phosphoinositide turnover by following the translocation of the pleckstrin homology domain of PLCδ1 fused to green fluorescent protein (PH-GFP). The observed time course could be simulated by incorporating binding of PIP_2 and $InsP_3$ to PH-GFP into the model that had been used to analyze the biochemistry. Furthermore, this analysis could help to resolve a controversy over whether the translocation of PH-GFP from membrane to cytosol is due to a decrease in PIP_2 on the membrane or an increase in $InsP_3$ in cytosol; by computationally clamping the concentrations of each of these compounds, the model shows how both contribute to the dynamics of probe translocation.

Introduction

Phosphatidylinositol 4,5-bisphosphate (PIP_2)* which represents <1% of membrane phospholipids, is the predominant (>99%) doubly phosphorylated phosphoinositide in mammalian cells (Vanhaesebroeck et al., 2001). It plays important roles in PLC-mediated cellular processes because hydrolysis of PIP_2 by PLC generates DAG and inositol 1,4,5-trisphosphate ($InsP_3$; Berridge and Irvine, 1984; Berridge, 1993), which serve as second messengers for intracellular Ca^{2+} mobilization and PKC activation, respectively. Recent papers show PIP_2 also plays important roles in membrane trafficking (Huijbregts et al., 2000; Manifava et al., 2001; Martin, 2001), interactions with cytoskeletons (Nebl et al., 2000; Rozelle et al., 2000; Sechi and Wehland, 2000; van Rheenen and Jalink, 2002), and modulation of ion transporters and channels (Czech, 2000; Hilgemann et al., 2001).

We have been interested in the activation of the PLC signaling pathway, particularly in a neuronal context, and have examined this extensively in a murine neuroblastoma cell line, N1E-115. In these cells, activation of the endogenously expressed bradykinin B2, a G protein–coupled receptor, results in a significant elevation of the intracellular $[Ca^{2+}]$ and $[InsP_3]$ (Fink et al., 1999a, 2000), and M current inhibition (Higashida and Brown, 1987). We have found that M current inhibition does depend on activation of PLC, but has much slower kinetics than either $InsP_3$ or Ca^{2+} (Xu and Loew, 2003). Also recently, it has been shown that membrane PIP_2 level plays an important role in M current modulation (Suh and Hille, 2002; Zhang et al., 2003).

Although $InsP_3$ increase is a direct consequence of PIP_2 hydrolysis induced by PLC activation, it was noted in several papers that the $InsP_3$ kinetics are generally more rapid compared with the decrease and subsequent recovery in membrane PIP_2 (Kaya et al., 1989; Willars et al., 1998). It should be pointed out that the level of cellular PIP_2 is actually regulated by the balance between the degradative and synthetic enzymes. The recovery of membrane PIP_2 is probably mediated by PIP_2 resynthesis at the plasma membrane. The majority of PIP_2 is synthesized via the sequential phosphorylation of phosphatidylinositol (PI) at the 4′ position by PI 4-kinases to produce PI 4-phosphate, and then at the 5′ position by

type I phosphoinositide 5-kinases (for reviews see Toker, 1998; Tolias and Cantley, 1999). Recently, it has been found that PIP_2 can also be synthesized via the phosphorylation of PI 5-phosphate at the $4'$ position by type II phosphoinositide 5-kinases (Rameh et al., 1997). On the other hand, other than PLC, the degradation of PIP_2 can be mediated either by PI 3-kinases or PIP_2 5-phosphatases such as synaptojanin (Mitchell et al., 1996; Nemoto et al., 1997; Sakisaka et al., 1997; Takenawa et al., 1999).

It has been noted that activation of PLC by α1-adrenergic and muscarinic agonists caused an increased ^{32}P incorporation into polyphospho-PIs in myocardium (Kiss and Farkas, 1975; Quist, 1982; Quist and Sanchez, 1983; Sekar and Roufogalis, 1984), as well as an increased generation of $InsP_3$ (Mitchell et al., 1981). Additionally, it has been found that both $InsP_3$ and PIP_2 increase at the time of fertilization in sea urchin, *Xenopus*, and mouse eggs (Turner et al., 1984; Ciapa et al., 1992; Stith et al., 1993, 1994; Snow et al., 1996; Halet et al., 2002), and during the stimulation of platelets with thrombin (Lassing and Lindberg 1990). All these findings suggest that hydrolysis and synthesis of plasma membrane PIP_2 may be tightly coupled such that PIP_2 synthesis rapidly compensates for, or is independently stimulated by, its hydrolysis. Moreover, Chahwala et al. (1987) found that the guanine nucleotide analogue guanosine $5'-O$-(3-thiotriphosphate) (GTPγS), which could stimulate G proteins, activated PLC in $[^3H]$inositol-labeled fibroblast cells. They also found that the GTPγS-induced increase in $InsP_3$ was 10 times over the decrease in PIP_2, suggesting that a stimulated PIP_2 synthesis by PI and PIP kinases might accompany activation of PLC.

Recently, a GFP fusion protein, which consists of the pleckstrin homology (PH) domain of PLCδ1 fused to GFP (PH-GFP), was developed as a probe for PIP_2 in single cells (Stauffer et al., 1998; Varnai and Balla, 1998). This indicator has a high affinity for PIP_2 and $InsP_3$ (Rebecchi et al., 1992; Lemmon et al., 1995; Kavran et al., 1998) because of multiple hydrogen bond formations between its PH domain residues and the 4-and 5-phosphates on the inositol ring (Ferguson et al., 1995). The expressed fluorescent probe predominantly associates with the plasma membrane in unstimulated cells (consistent with the distribution of PIP_2 in mammalian cells), and translocates to the cytosol on activation of PLC. Because PLCδ-PH shows 10–20-fold higher affinity for $InsP_3$ than PIP_2 in vitro (Hirose et al., 1999; McLaughlin et al., 2002), there are disputes about whether the translocation of PH-GFP from membrane to cytosol is due to a decrease in membrane PIP_2 level or an increase in cytosolic $InsP_3$. Although Halet et al. (2002) and van der Wal et al. (2001) showed that 10–100 μM of photoreleased $InsP_3$ was required to induce the translocation of PH-GFP from the plasma membrane, suggesting physiological increases of $InsP_3$ on activation of PLC (e.g., 3 μM in N1E-115 cells, Fink et al., 1999a, 2000; or 0.3 μM in smooth muscle cells, Fink et al., 1999b) could not be solely responsible for translocation of PH-GFP; Hirose et al. (1999) found intracellular injection of small amount of $InsP_3$ (<10 μM) caused significant translocation of PH-GFP; they also showed that rapid degradation of $InsP_3$ by overexpression of an $InsP_3$ 5-phosphatase abolished ago-

nist-induced PH-GFP translocation (Hirose et al., 1999; Okubo et al., 2001), suggesting translocation of PH-GFP was monitoring changes in $InsP_3$.

In this paper, we compared biochemical experiments measuring the kinetics of the bradykinin-induced changes in PIP_2 mass in suspensions of N1E-115 neuroblastoma cells with the results of single-cell measurements of PH-GFP translocation. This extends our earlier work on the bradykinin-induced $InsP_3$ and Ca^{2+} dynamics in these cells (Fink et al., 1999a, 2000). In these works, we make extensive use of the "Virtual Cell" modeling environment (Schaff et al., 1997, 2001; Loew and Schaff 2001; Slepchenko et al., 2002) to analyze the data and to develop a quantitative mechanistic understanding of the system. We show that the analysis predicts, and subsequent experiments confirm, an initial stimulated increase in PIP_2 concomitant with activation of PLC-mediated PIP_2 hydrolysis. Furthermore, the kinetic analysis offers an approach toward reconciling the conflicting works on the behavior of PH-GFP.

Results

Phosphoinositide content in N1E-115 cells

Phosphoinositides, the majority of which include PI, lyso-PI, PI 4-phosphate, and PIP_2, are minor constituents of membrane lipids in eukaryotic cells, yet play important roles in signal transduction (Berridge and Irvine, 1984; Payrastre et al., 2001). First, we determined the $[^3H]$inositol incorporation into phosphoinositides that were separated on oxalate-impregnated silica gel thin-layer plates using a developing solvent system of chloroform/methanol/4 N NH_4OH (45:35:10, vol/vol/vol). Over the first 24 h, incubation of N1E-115 cells with $[^3H]$inositol led to marked changes in the distribution of ^3H radioactivity in PI, lyso-PI, PIP, and PIP_2 under unstimulated conditions (unpublished data). However, no significant differences between cells labeled for 24, 44, 48, or 52 h were found under either unstimulated or stimulated conditions (unpublished data). Therefore, the phosphoinositide pools were believed to be in equilibrium after 48 h incubation with $[^3H]$inositol. As shown in Table I, the Rf values of the four major phosphoinositides were consistent with the Rf values previously reported (Gonzalez-Sastre and Folch-Pi, 1968; Racagni et al., 1992). The relative distribution of ^3H radioactivity in PI, lyso-PI, PIP, and PIP_2 in the unstimulated N1E-115 cells prelabeled with $[^3H]$inositol for 48 h is also shown in Table I. Although $[^3H]$PI was the major component of the $[^3H]$phosphoinositide (85.4 $\pm$ 2.8%), $[^3H]PIP_2$ and

Table I. **Relative levels and Rfs of $[^3H]$phosphoinositides in $[^3H]$inositol-prelabeled N1E-115 cells determined by TLC**

	Radioactivity	Rf
PI	100 $\pm$ 0	0.49 $\pm$ 0.02
Lyso-PI	12.6 $\pm$ 3.0	0.41 $\pm$ 0.02
PIP	2.4 $\pm$ 0.3	0.27 $\pm$ 0.01
PIP_2	2.8 $\pm$ 0.8	0.11 $\pm$ 0.02

$[^3H]$phosphoinositide distribution in $[^3H]$inositol-prelabeled N1E-115 cells was prepared and analyzed as described in Materials and methods. Values shown are mean $\pm$ SEM of seven experiments.

[³H]PIP only represented $2.3 \pm 0.6\%$ and $2.0 \pm 0.2\%$, respectively ($n = 7$). When labeled to equilibrium by [³H]inositol, [³H]phosphoinositides have a similar distribution as the endogenous inositol lipids (Kaya et al., 1989). Therefore, our paper indicates that PI is the most abundant phosphoinositide in N1E-115 cells, whereas PIP and PIP₂ occur in trace amounts only.

To examine the relative content of PIP₂ in the cell membrane, cells were labeled to equilibrium with [³²P]PO₄²⁻. We used the same TLC system as described in the previous paragraph to resolve PIP₂ from the other phosphoinositides (PI, PI 4-phosphate) and all other plasma membrane phospholipids (Gonzalez-Sastre and Folch-Pi, 1968). Our data showed that PIP₂ comprised $0.43 \pm 0.02\%$ of total cellular phospholipids. We assume 50% of total cellular phospholipids are present in the plasma membrane (Lange et al., 1989; Warnock et al., 1993). Additionally, recent evidence from one cell line indicates that ~40% of total cellular PIP₂ is present in the plasma membrane (Watt et al., 2002). Thus, the basal level of PIP₂ can be estimated at 0.3% of phospholipids in the plasma membrane. Furthermore, the percentage of PIP₂ relative to the phospholipids in the inner leaflet of the plasma membrane would be 0.5% because 80% of PIP₂ is found in the inner leaflet of the plasma membrane. Assuming that phospholipids cover 60% of the inner surface (Jain, 1980), and that a single lipid molecule occupies 70Å² (McLaughlin et al., 1981), a surface density of 4,000 molecules/μm² for PIP₂ can be estimated. This will be taken as the basal level of PIP₂; the basal levels of the other inositides can then be calculated from Table I.
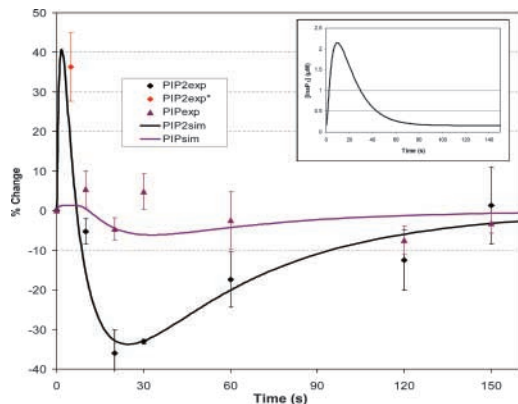
Bradykinin-induced decrease in membrane PIP₂ level

On addition of a 1-μM concentration of bradykinin that is maximal for the bradykinin receptor-mediated InsP₃ generation (Fink et al., 1999a, 2000), there was a relative decrease of PIP₂ (Fig. 1, black diamonds), which was detectable by 10 s, and reached a minimum ($-36.0 \pm 6.0\%$, $n = 5$) by 20 s. Levels of [³H]PIP₂ recovered to basal levels in ~150 s in the continued presence of bradykinin. The rate of recovery of PIP₂ was much slower than that of InsP₃, which reaches its maximum before 10 s and returns to basal levels by 30 s at 37°C (Fink et al., 1999a, 2000). Also shown in Fig. 1 are the experimental data for PIP, which show relatively little change after bradykinin stimulation.

It should be mentioned that, in some earlier works, absolute PIP₂ mass was determined by assay of InsP₃ released by alkaline hydrolysis (Willars et al., 1998). In our work, [³H]PIP₂ mass was determined from the radioactivity of the PIP₂ spot on a silica gel TLC plate (Kaya et al., 1989; Racagni et al., 1992; Lukacova and Marsala, 1997), which might contain radioactivity from other doubly phosphorylated phos-
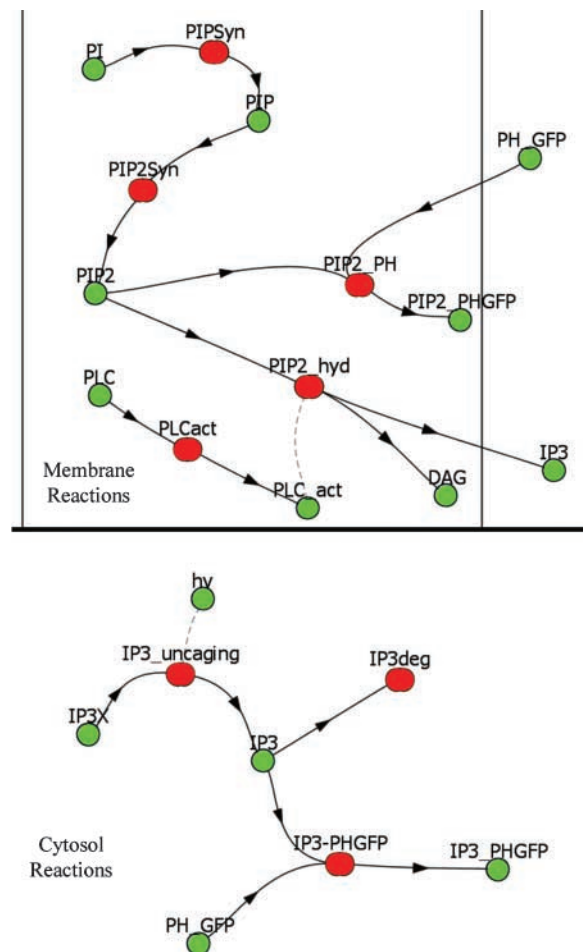
Figure 1. **Experimental and simulated time courses of bradykinin-induced changes of PIP₂ and PIP in N1E-115 cells.** [³H]inositol-prelabeled N1E-115 cells were incubated in the presence of 1 μM bradykinin for the indicated times. Membrane lipids were extracted and analyzed as described in Materials and methods. Each data point is the mean ± SEM of three to five experiments. All experiments were performed at RT. Black diamonds represent our initial determination of PIP₂ changes; purple triangles are the PIP data. These data, along with our prior study of InsP₃ dynamics in this cell, were used to constrain a model that produced the respective black and purple solid curves. The pathways that were modeled are shown in Fig. 2, and the model equations and parameters are described in the Appendix. The prediction of the model that there was an initial increase in [PIP₂] led us to determine the change in PIP₂ at 5 s, shown as a red diamond. The model calculation of the change in [InsP₃] is shown in the inset.

Figure 2. **Reaction scheme for the synthesis and hydrolysis of PIP₂.** The membrane-associated reactions are shown at the top, and the cytosol reactions on the bottom. These reaction schemes form the basis of the mathematical models that were developed to analyze the data. Details of the rate expressions for each of the reactions (shown in red) are provided in the Appendix.

phoinositides such as PI 3,4-bisphosphate. However, because PIP_2 is the predominant (>99%) doubly phosphorylated phosphoinositide in mammalian cells (Vanhaesebroeck et al., 2001), the contribution to $[^3H]PI(4,5)P_2$ radioactivity from $[^3H]PI(3,4)$-bisphosphate should be negligible.

Bradykinin stimulates membrane PIP_2 synthesis, resulting in an initial increase in PIP_2

We analyzed the experiments in Fig. 1 using the Virtual Cell software with a simple model consisting of a transient activation of PLC-mediated PIP_2 hydrolysis followed by a slow recovery to basal levels via phosphorylation of PI and PIP (Fig. 2). Mathematical details of the model are provided in the Appendix, along with a list of the parameters and how they were chosen. The results of the simulation are shown in Fig. 1 so as to permit ready comparison to the experiment.

A key constraint on the model was the previously determined level and kinetics of $InsP_3$ produced during bradykinin-induced activation of PLC. Previous findings in this lab indicated that bradykinin-induced generation of $InsP_3$ in N1E-115 cells reached its peak of several µM before 10 s (Fink et al., 1999a, 2000). This previous work used quantitative photorelease of caged $InsP_3$ and calcium imaging to establish the amount of $InsP_3$ required to attain a level of calcium release equivalent to that obtained with maximal stimulation with bradykinin. We also directly determined the bradykinin-induced $InsP_3$ kinetics using a combination of modeling and direct biochemical $InsP_3$ mass determinations. In the present model, we adjusted some of the parameters to reflect the slower kinetics of bradykinin-induced calcium dynamics (Xu and Loew, 2003) and slower $InsP_3$ degradation at RT. But our experimentally determined decrease of PIP_2 simply couldn't account for sufficient $InsP_3$ unless a stimulated synthesis of PIP_2 was resupplying this substrate. This stimulated synthesis was added to the model using PIP as the required precursor. However, because basal PIP was itself even lower than PIP_2 (Table I), PIP resupply through stimulated phosphorylation of PI also had to be incorporated into the model. PI is in abundant supply, so its depletion is insignificant and would not affect the kinetics of either PIP or PIP_2.

The resultant model predicted a transient increase of PIP_2 at times earlier than our initial experimental time points (Fig. 1, the rise of the black simulation curve above the baseline between 0 and 8 s). To investigate this possibility, we measured the bradykinin-induced change in $[^3H]PIP_2$ at 5 s. Indeed, we found that bradykinin caused a relative increase in $[^3H]PIP_2$ (36.3 ± 8.6%, $n = 3$) compared with that before stimulation (Fig. 1, red diamond). To confirm that the increase in PIP_2 is due to PIP_2 synthesis, we pretreated the cells with micromolar wortmannin (30 µM, 15 min). Wortmannin at nanomolar concentrations inhibits PI 3-kinases, but at micromolar concentrations, it also inhibits the activity of most PI 4-kinases (Nakanishi et al., 1995; Downing et al., 1996). In cells treated with wortmannin, the increase in $[^3H]PIP_2$ at 5 s was abolished; instead, a relative decrease in membrane PIP_2 (−5.1 ± 1.1%, $n = 4$) was obtained.

Bradykinin-induced PH-GFP translocation

Knowing that the kinetics of bradykinin-induced decrease in membrane PIP_2 and increase in cytosolic $InsP_3$ were very different in terms of both time-to-peak and recovery, we tried to determine whether PH-GFP translocation mimicked changes in PIP2 or InsP3 in single cells. When expressed in N1E-115 cells, PH-GFP showed a strong accumulation at the plasma membrane and a low and homogenous distribution in the cytosol (Fig. 3), consistent with the idea that PH-GFP primarily binds to membrane PIP_2 at rest. Several explanations for the low resting intracellular PH-GFP fluorescence are possible: (1) intracellular pools of PIP_2 are not accessible to PH-GFP (Balla et al., 2000); (2) some intracellular PIP_2 phosphatases (e.g., synaptojanin) have hydrolyzed the PIP_2 on the internal membranes and restricted the steady-state accumulation of PIP_2 to the plasma membrane (Stefan et al., 2002); or (3) a significant amount of PIP_2 is on the organelle membranes and can bind PH-GFP (Watt et al., 2002), but its lower volumetric density compared with the plasma membrane produces a lower fluorescence. In this work, we measured fluorescence from membrane GFP, segmented by a combination of threshold operations and manual editing, and cytosolic fluorescence regions of interest individually for each time point; we did not use the more common procedure of measuring the amplitude of the fluorescence signal at the plasma membrane and cytosol region along a line across the cell for all time points because we found that bradykinin could induce cell shape changes, and hence, changes of the originally assigned membrane regions. After addition of bradykinin, there was a decrease in plasma membrane PH-GFP fluorescence and a concomitant increase in cytosolic fluorescence (Fig. 3 and Fig. 4). The maximum relative change in membrane GFP fluorescence was −11.3 ± 1.7% ($n = 19$), whereas the relative change in cytosolic fluorescence was 41.1 ± 4.7% ($n = 19$). The kinetics of bradykinin-induced PH-GFP translocation is characterized by a rapid onset, with translocation peaking at ∼20 to 30 s and returning to the baseline in ∼3 min in the continued presence of brady-
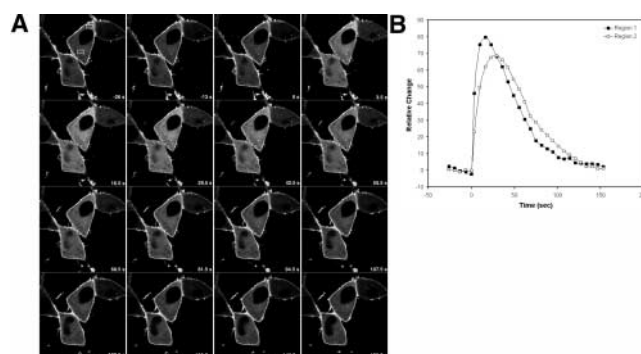

Figure 3. **Bradykinin-induced translocation of PH-GFP from the plasma membrane in a single N1E-115 cell.** A single N1E-115 cell was stimulated with 1 µM bradykinin. PH-GFP translocation was reflected as a decrease in the membrane GFP fluorescence and a concomitant increase in cytosolic fluorescence. The experiment was performed at RT. (A) Time series of images with the time indicated on each frame in seconds. Bradykinin was added at time 0 (after the third frame). (B) Relative change in GFP fluorescence at two locations in the cytosol of the cell in the images in A. Region 1 is indicated in the first frame of A by the rectangle just above the nucleus; region 2 is indicated by the rectangle in the larger area of cytosol below the nucleus.
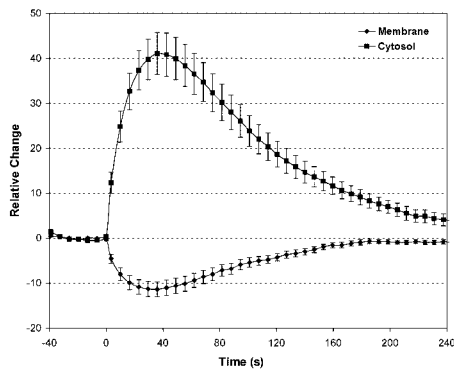
Figure 4.   **Kinetics of bradykinin-induced PH-GFP translocation.** The average changes in membrane and cytosol fluorescence after addition of 1 μM bradykinin are plotted versus time. Each point was the mean ± SEM of 19 experiments.
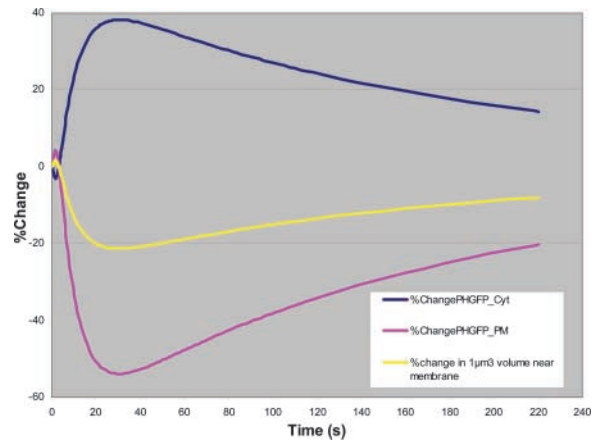

Figure 5.   **Simulation of PH-GFP translocation.** The compartmental model used in Fig. 1 was expanded to include PH-GFP binding. Additional parameters are in Table AII, and model equations are in the Appendix. The blue curve represents the relative change in total cytosolic GFP (free PH-GFP + InsP$_3$–PH-GFP), and can be directly compared with the corresponding experimental results in Fig. 4. The pink curve corresponds to the relative change in PIP$_2$–PH-GFP surface density on the plasma membrane. Because the confocal imaging system detects both fluorescence from the membrane and the adjacent cytosol, the PIP$_2$–PH-GFP results were adjusted by an appropriate contribution from the total cytosolic signal in the yellow curve, as detailed in the text, to allow comparison with the experimental result in Fig. 4.

kinin (Fig. 3). This time course is very similar to the time course of PIP$_2$ hydrolysis detected biochemically from [^{3}H]inositol-labeled cells, in line with the previous finding that PH-GFP translocation primarily reports changes in membrane PIP$_2$ content (van der Wal et al., 2001). However, the bradykinin-induced PH-GFP translocation did not exhibit an initial increase in PIP$_2$, raising the possibility that PH-GFP translocation might not be determined solely by changes in membrane PIP$_2$.

The expression level of PH-GFP may be an important factor in determining the extent to which membrane PIP$_2$ and cytosolic InsP$_3$ affect the distribution of the PH-GFP. We estimated intracellular GFP concentrations by comparing the cytosolic fluorescence intensities of individual cells in situ to those of a series of dilutions of purified GFP protein of known concentration (see Materials and methods). The basal levels of cytosolic PH-GFP ranged from 3 to 12 μM, with an average of 5.9 ± 0.5 μM (n = 19). However, we did not find any significant correlation between the basal cytosolic PH-GFP concentration and either the time constants or the amplitudes of the bradykinin-induced PH-GFP translocation, possibly because the range of PH-GFP expression levels was not sufficient.

We elaborated the model used to analyze the biochemical data on inositide turnover to see if it could also predict the PH-GFP translocation experiments. The basal concentration of total PH-GFP in the cytosol (free plus bound to InsP$_3$) was taken as 6 μM from our measurements. Binding constants to InsP$_3$ and PIP$_2$ were taken from in vitro measurements reported in the literature (Hirose et al., 1999). Taken with the basal levels of InsP$_3$ and PIP$_2$, these determined the basal levels of the bound forms of PH-GFP. Thus, all the additional model parameters were completely based on measured values (albeit in vitro), and no parameters were adjusted to fit the results of Fig. 4. All these parameters are provided in Table AII of the Appendix. The results of a compartmental model, elaborated from the one used in Fig. 1, are shown in Fig. 5. The results of a two-dimensional spatial simulation, based on the geometry of one of the cells of Fig. 3, are shown in Fig. 6.

The change in the cytosolic concentration in Fig. 5 and the top row of Fig. 6 can be directly compared with the cor-

responding experimental results in Fig. 4 and Fig. 3, respectively; this is because the intensity measured within a confocal volume correctly reflects the concentration of a fluorophore whenever the confocal voxel is well within the volume of the container that surrounds the fluorophore, i.e., the volume contained by the cell (Fink et al., 1998). We estimate our confocal volume to be ∼0.7 × 0.7 μm within the focal plane, and 2.1 μm in the axial dimension. In our experiments, we placed the focal plane near the center of the cell, and the cell dimensions are significantly larger than the confocal volume. However, this same consideration precludes direct comparison of the measured fluorescence change from the cell periphery and the simulation results from the plasma membrane (Fig. 5, pink curve; Fig. 6, second row). The confocal volume encompassing the thin monolayer of membrane fluorescence also contains essentially all of the adjacent cytosolic fluorescence. To account for this, we estimated the total PH-GFP species within a 1-μm^3 (0.7 × 0.7 × 2.1 μm^3) volume encompassing the membrane by adding the PIP$_2$–PH-GFP molecules in a vertical patch of membrane 0.7 × 2.1 μm^2 to the PH-GFP and IP$_3$–PH-GFP in a 0.7 × 0.7 × 2.1 μm^3 region adjacent to the membrane. The relative change of this quantity is depicted in yellow in Fig. 5.

As can be seen, all three curves in Fig. 5 show that the simulated translocation of PH-GFP only slightly reflects the initial increase in PIP$_2$ determined from both the model and the experiment of Fig. 1. Of course, this initial increase is still present in the simulation results for unbound PIP$_2$ in the presence of PH-GFP (shown for the spatial simulation in Fig. 6). Indeed, the fact that the simulation results in Fig. 5 and Fig. 6 for the PH-GFP translocation are reasonably
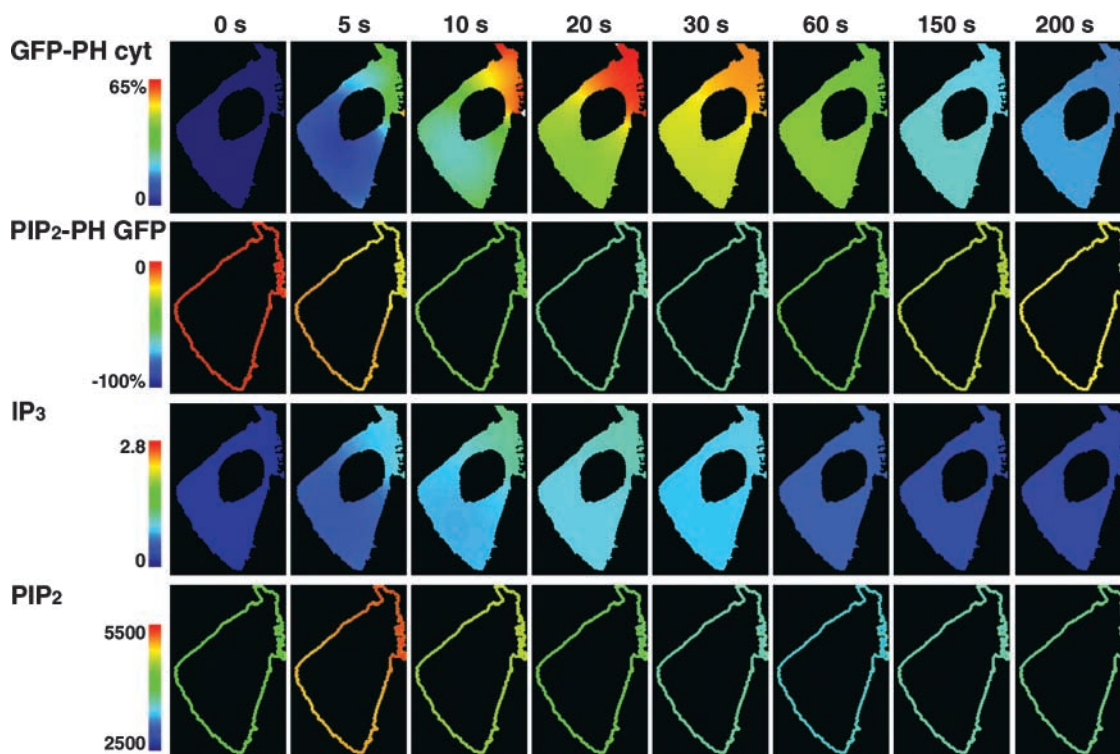
Figure 6. **Results of an image-based spatial simulation of PH-GFP translocation after bradykinin-induced stimulation.** The image of the cell on the right side of the images in Fig. 3 was used as the basis of the two-dimensional geometry. The cytosolic resting level of PH-GFP that was measured for this cell was 4.6 μM, and this was the value used in the simulation. Other parameters were similar to the compartmental simulations (Table AI and Table AII). Details of the simulation are given in the Appendix. (Top row) Selected time points for the relative changes in total cytosolic PH-GFP (free + bound to InsP$_3$). (Second row) Percent change in PH-GFP associated with PIP$_2$ in the plasma membrane. (Third row) Concentration of free InsP$_3$, indicated by the color bar in unit of μM, in the cytosol showing the buffering effect of PH-GFP as described in the text. (Fourth row) Surface density of PIP$_2$, indicated by the color scale in molecules/μm^2, also showing the buffering effect of the indicator.

close to the experimental observations in Fig. 3 and Fig. 4 provides additional support for the overall model. Of course, there are some discrepancies, and it would be important to explore potential sources of error in the model. The most important implicit assumptions in the model are that PH-GFP–bound forms of both InsP$_3$ and PIP$_2$ are protected from degradation. That is, as shown in Fig. 2, PIP$_2$–PH-GFP does not directly hydrolyze to InsP$_3$, and IP$_3$–PH-GFP does not directly become degraded. This has the effect of slowing inositide turnover by sequestering a dynamic fraction in the PH-GFP bound forms. That the turnover of these molecules is inhibited by PH-GFP is clear (Varnai and Balla 1998), but that the extent of inhibition is complete in both bound form may be an oversimplification. The assumption of complete inhibition of InsP$_3$ degradation in the bound form is probably the primary source of the slower recovery of translocation in the simulation compared with the experiment. Clearly, another important approximation of the model is the application of in vitro biochemically determined Kd's for binding of PH-GFP to InsP$_3$ and PIP$_2$ to an analysis of in vivo experiments, but no in vivo measurements are available. Additionally, the possibility of special binding mechanisms in vivo has recently been suggested to explain the different binding behavior of various PH isoforms (Varnai et al., 2002).

The results for the PH-GFP translocation in the spatial model (Fig. 6, top row) also capture the features of the ex-

perimental results from that cell (Fig. 3, right-hand cell). In particular, the nucleus creates a small diffusion barrier that effectively creates a high surface-to-volume region of cytosol to its upper right compared with the larger cytosolic region below the nucleus. The nuclear diffusion barrier creates a temporary buildup of released PH-GFP in the upper right that is seen both experimentally (Fig. 3 B, compare the respective plots for region 1 and 2) and in the simulation (Fig. 6; namely, the faster and higher rise of PH-GFP in that region of the cell revealed by the pseudocolor display in the top row).

It is also instructive to compare the changes in PIP$_2$ and InsP$_3$ in the presence of PH-GFP, shown in the bottom two rows of Fig. 6, with the changes that the model calculates when the PH-GFP is removed, shown in Fig. 7. The simulation results in Fig. 7 are the result of simply setting the concentrations of all of the PH-GFP molecular species to zero and are mathematically equivalent to the application of the nonspatial model of Fig. 1 to our two-dimensional geometry. As can be seen, both the rates and the amplitudes of the changes in InsP$_3$ and PIP$_2$ are severely reduced in the presence of 6 μM PH-GFP, which effectively acts as a buffer for both of these molecules. These simulations suggest that caution is required in interpreting the physiology of PH-GFP–transfected cells. Indeed, the ability of PH-GFP to impede access of PLC to PIP$_2$ was recognized in one of the original papers that described this probe (Varnai and Balla, 1998).
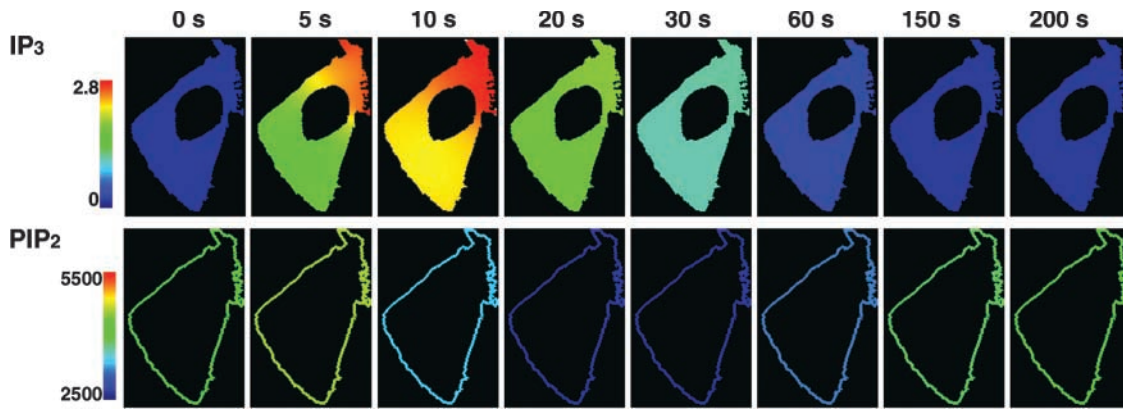
Figure 7.   **Results of an image-based spatial simulation of phosphoinositide turnover after bradykinin-induced stimulation.** The simulations were performed as in Fig. 6, except that PH-GFP was not included in the system. (Top row) Concentration of InsP$_3$ in the cytosol. (Second row) Selected time points for the surface density of PIP$_2$. The same scales were used as in the bottom two rows of Fig. 6 to facilitate comparison.

Whether PHδ1-GFP inhibits InsP$_3$-dependent calcium release has not been reported to our knowledge, although it has been reported for another PH domain isoform (Varnai et al., 2002).

Is PH-GFP translocation reporting changes in PIP$_2$ or InsP$_3$?

There has been considerable uncertainty in the literature as to whether PH-GFP translocation monitors changes in PIP$_2$ or InsP$_3$ (Hirose et al., 1999; van der Wal et al., 2001). Physiologically, a decrease in PIP$_2$ will be accompanied by an increase in InsP$_3$, so it is difficult to know which is the primary source for translocation of the probe from the plasma membrane to the cytosol. Experiments where the concentration of one molecule is clamped while the other molecule is changed can give seemingly contradictory results. For example, microinjection of InsP$_3$ led to translocation (Hirose et al., 1999), whereas photorelease of similar intracellular concentrations from a caged precursor (van der Wal et al., 2001) did not.

However, in our mathematical model, we can design thought experiments in which each of these molecules is clamped at its initial concentration, and then perform simulations to see how the system would respond to the bradykinin stimulus. The changes in total cytosolic PH-GFP from such calculations are shown in Fig. 8, with the results for the regular compartmental model shown for comparison. The calculation labeled "Fixed InsP$_3$" included all the reactions in the regular model, but the concentration of InsP$_3$ in the cytosol was clamped to its initial value of 0.16 μM; this is equivalent to introducing a new InsP$_3$ degradation mechanism with a perfect feedback control to assure a rate that is precisely tuned to maintain 0.16 μM at all rates of PIP$_2$ hydrolysis. Similarly, the calculation labeled "Fixed PIP$_2$" clamps the PIP$_2$ surface density at its initial value of 4,000 molecules/μm^2, while allowing InsP$_3$ production to proceed at a rate identical to that in the regular model. As can be seen, both of these circumstances produce significant translocation of the probe, suggesting that PH-GFP translocation is independently sensitive to both changes in PIP$_2$ and InsP$_3$. Of the two cases, the change in InsP$_3$ (i.e., clamped PIP$_2$) produces a PH-GFP translocation that is closer to that pro-

duced by the full simulation. However, it should be emphasized that these results would be particularly sensitive to the relative affinities of the probe for InsP$_3$ vs. PIP$_2$, and again the values were taken from in vitro experiments.

We also used the model to examine the contrasting results that were reported when InsP$_3$ is introduced into cells in the absence of receptor-mediated activation of PLC. Hirose et al. (1999) reported that injection of 1 μM InsP$_3$ could produce large translocation of PH-GFP, whereas van der Wal et al. (2001) used photorelease of caged InsP$_3$ to reach the opposite conclusion. Fig. 9 shows a series of simulations of the translocation response to a 1-μM instantaneous bolus of InsP$_3$ at time 0 in the absence of phosphoinositide turnover. The three traces correspond to differing initial concentrations of total cytosolic PH-GFP, with the central concentration (6 μM) corresponding to the average concentration of the probe measured in our experiments. As can be seen, the translocation produced by 1 μM InsP$_3$ in the presence of 6 μM total cytosolic PH-GFP is predicted to be much smaller than that pro-
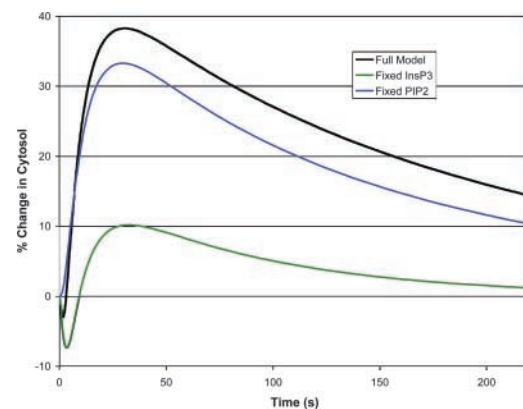

Figure 8.   **Compartmental simulations with fixed InsP$_3$ or PIP$_2$.** The model of Fig. 5 was used, except that InsP$_3$ (green) or PIP$_2$ (blue) are clamped at their initial values. Only the change in total cytosolic PH-GFP is shown because this is the only model output that may be directly compared with the corresponding experimental result (shown in Fig. 4) as explained in the text. Also shown for comparison is the result produced by the full model in which all molecules are allowed to vary (black curve).
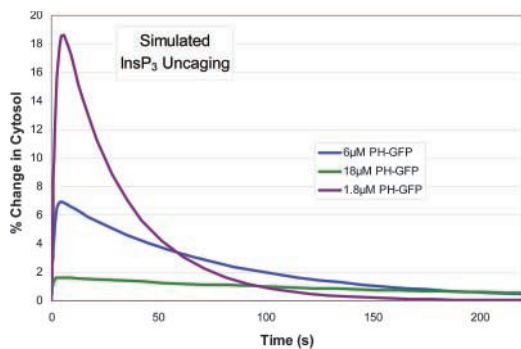
Figure 9. **Compartmental simulation of the response of the steady-state system to an instantaneous bolus of 1 μM InsP$_3$.** The same compartmental model was used, except that the bradykinin stimulus was never applied. Instead, InsP$_3$ was stepped from the basal level of 0.16 μM to 1.16 μM at time 0. This was equivalent to a rapid injection or a pulse of photorelease. The response of PH-GFP translocation is displayed for three initial total cytosolic concentrations of the indicator. The central value of 6 μM (blue curve) corresponds to the average expression level in our cells.

duced in the full model of receptor-activated phosphoinositide turnover (Fig. 8, black trace). However, the effect is very sensitive to the expression level of the indicator over a 10-fold range. Hirose et al. (1999) and van der Wal et al. (2001) did not report the concentrations of indicator in their respective experiments. So, the difference in their results may be a consequence of a low PH-GFP expression level in the former and a high expression level in the latter. In conclusion, our results suggest that the relative or percent change in translocation after stimulated phosphoinositide turnover will be higher with lower concentrations of PH-GFP, when the PH-GFP will not buffer a significant fraction of either membrane PIP$_2$ or cytosolic IP$_3$. However, at very low concentrations, the intensity of the fluorescence may, of course, become limiting.

Discussion

In this paper, we showed that bradykinin induced first an increase, then a decrease, in membrane PIP$_2$ in N1E-115 neuroblastoma cells. Micromolar wortmannin, which blocks most PI 4-kinases (Nakanishi et al., 1995; Downing et al., 1996) and PI 3-kinases, completely abolished the initial increase and even revealed an immediate decrease in PIP$_2$. Because PI 4-kinases are required for PIP$_2$ synthesis, these results could indicate that bradykinin leads to a rapid activation of PIP$_2$-synthesizing kinases, and that this effect precedes the hydrolysis of PIP$_2$ mediated by PLC. The rapid synthesis of PIP$_2$ can also explain why the maximum decrease in PIP$_2$ occurs at 20 s, 10 s behind the maximum increase in both InsP$_3$ and intracellular Ca^{2+} concentration (Fink et al., 1999a, 2000; Xu and Loew, 2003). Bradykinin binds to B$_2$ receptor (Coggan and Thompson, 1995, 1997) in N1E-115 cells, which use a GTP-binding protein, G$_q$, to activate phospholipase Cβ1. Whether bradykinin uses the same signal pathway to activate PI 4-kinase and PLC is not known. It should be pointed out, though, that a decrease in the activity of PIP$_2$ phosphatases could also lead to an increase of PIP$_2$. Whether bradykinin inhibits PIP$_2$ phosphatase in N1E-115 cells remains to be determined.

Consistent with our findings, Yorek et al. (1994) found that bradykinin stimulated ^{32}P incorporation into PIP and PIP$_2$ as well as InsP$_3$ release in neuroblastoma cells. Similarly, it was found that binding of thrombin to its receptors caused a synthesis of PIP and PIP$_2$, preceded by degradation of these phosphoinositides in platelets (Lassing and Lindberg, 1990). In fibroblasts, net synthesis of the phosphoinositides was revealed when hydrolysis of PIP$_2$ was blocked by neomycin (Carney et al., 1985). Also in fibroblasts, Chahwala et al. (1987) found that the GTPγS-stimulated hydrolysis of PIP$_2$ concomitant with an increase in InsP$_3$ that was 10 times over the decrease in PIP$_2$, suggesting PIP$_2$ synthesis was also accelerated after GTPγS addition. In a very different system, it was shown in sea urchin (Turner et al., 1984) and *Xenopus* (Snow et al., 1996) eggs that inositol lipid levels increased on fertilization, but this may be due to a later event associated with cortical granule exocytosis, as has been recently shown for mouse egg fertilization (Halet et al., 2002). In any case, the generality of a concurrent receptor-mediated stimulation of PIP$_2$ hydrolysis and synthesis is certainly not established. This may be because the early transient nature of the phenomenon, as well as its unexpectedness, has made it elusive.

We further investigated the turnover of phosphoinositides by following the translocation of PH-GFP. In unstimulated cells, the PH-GFP was concentrated at the plasma membrane as seen before (Stauffer et al., 1998; Varnai and Balla, 1998; Holz et al., 2000; van der Wal et al., 2001), indicating it preferentially binds to the plasma membrane PIP$_2$, possibly because there is a much higher cellular concentration of PIP$_2$ in the plasma membrane (4 μM in our cells and $\sim$10 μM in general; McLaughlin et al., 2002) than cytosolic InsP$_3$ in N1E-115 cells (0.16 μM; Fink et al., 1999a). PH-GFP translocation induced by bradykinin showed similar kinetics as the membrane PIP$_2$ change measured by TLC, consistent with the finding of van der Wal et al. (2001) that PH-GFP primarily reported membrane PIP$_2$. However, the initial increase in membrane PIP$_2$ was not reflected in PH-GFP translocation. There may be several explanations for this discrepancy. First, overexpression of PH-GFP may interfere with cellular signals and inhibit synthesis of PIP$_2$. However, simultaneous recording of PH-GFP translocation and intracellular Ca^{2+} in N1E-115 cells showed that PH-GFP translocation also lagged behind the increase in intracellular Ca^{2+} induced by bradykinin (van der Wal et al., 2001), which correlated spatiotemporally with the InsP$_3$ increase (Fink et al., 1999a, 2000), suggesting synthesis of PIP$_2$ was still stimulated in the presence of PH-GFP. Another possible explanation is that PH-GFP translocation can be affected by both membrane PIP$_2$ and cytosolic InsP$_3$, and the translocation induced by the initial synthesis of PIP$_2$ is masked by binding of PH-GFP to increased InsP$_3$. There is compelling evidence that PH-GFP can monitor InsP$_3$ under some circumstances (Hirose et al., 1999; Nash et al., 2001; Okubo et al., 2001) in that the amount of InsP$_3$ increase produced by PIP$_2$ hydrolysis is by itself sufficient to induce PH-GFP translocation. However, in the work of van der Wal et al. (2001), it was found that interfering with PIP$_2$ resynthesis, but not InsP$_3$ generation, changed the kinetics of PH-GFP translocation in N1E-115 cells; this supports the

idea that PH-GFP monitors PIP$_2$. In both our experiments (Fig. 4) and simulations (Fig. 5), the initial fast increase in PIP$_2$ is not reflected in the PH-GFP translocation, but the overall time course does more closely resemble the behavior of PIP$_2$ than InsP$_3$.

A thorough analysis of the model helped to resolve some of these apparent contradictions, showing that PH-GFP translocation is sensitive to physiologically relevant changes in both InsP$_3$ and PIP$_2$. First, the model results for PH-GFP translocation (Fig. 5 and Fig. 6) produce reasonably good agreement with the experiment (Fig. 3 and Fig. 4). Because the parameters associated with PH-GFP binding to InsP$_3$ and PIP$_2$ were taken directly from the literature, and no parameters were adjusted to accommodate the incorporation of PH-GFP translocation into the phosphoinositide turnover model of Fig. 1, the close agreement between experiment and simulation is further support for the hypotheses that underlie the model. The model does reveal that translocation is sensitive to both InsP$_3$ and PIP$_2$ (Fig. 8), and that the presence of the indicator distorts the amplitude and time course of changes in both of these molecules through a buffering effect (compare Fig. 6 with Fig. 7). That this buffering effect can, in turn, severely diminish the sensitivity of the translocation to changes in phosphoinositide levels was illustrated in Fig. 9, where a 1-μM change in InsP$_3$ was calculated to give an insignificant translocation at high PH-GFP concentrations. Therefore, we suggest the expressed PH-GFP be kept at low concentrations so as not to buffer a significant fraction of either PIP$_2$ or IP$_3$. By highlighting the sensitivity of the assay to PH-GFP expression level, Fig. 9 could also help to explain the apparent conflicts in the literature on the amount of translocation elicited by InsP$_3$ alone (e.g., Hirose et al., 1999; van der Wal et al., 2001). It should also be pointed out that the receptor-mediated PLC activation may produce vastly differing amounts of InsP$_3$ for a given change in PIP$_2$ surface density in the plasma membrane in different cell lines. This would depend on the surface-to-volume ratio and the contribution of stimulated PIP$_2$ synthesis. For example, we have shown that bradykinin stimulates only a few hundred nM InsP$_3$ in a smooth muscle cell line even though this is still sufficient to elicit robust calcium release from the ER (Fink et al., 1999b). With differing initial concentrations and differing surface-to-volume ratios, the translocation behavior of PH-GFP would have to be analyzed for each cell system to dissect the sensitivity to PIP$_2$ vs. InsP$_3$.

We wish to conclude by emphasizing that this paper exemplifies the value of combining quantitative models with quantitative experiments. The initial results of our TLC experiments (Fig. 1, black diamonds) could only be fit to a model that predicted an initial increase in PIP$_2$. The hypothesis that was generated from this modeling result then prompted us to take an additional early experimental time point (Fig. 1; red diamond) that confirmed the prediction. But additional experiments using the PH-GFP translocation assay on individual cells (Fig. 3 and Fig. 4) failed to reveal this initial increase in PIP$_2$. However, an expanded model that included binding of PH-GFP to both PIP$_2$ and InsP$_3$ based on in vitro literature binding constants (Fig. 5 and Fig. 6) was largely consistent with the experiments, fail-

ing also to reveal an initial increase in PH-GFP association with the membrane even though the initial increase in PIP$_2$ was still present. Thus, the modeling result showed that the PH-GFP translocation experiment could not be used to argue against our initial hypothesis; indeed, it further supported it. Once we had this model, we could use it to visualize molecules that were not accessible experimentally (the spatiotemporal cellular distribution of PIP$_2$ and InsP$_3$ either in the presence, Fig. 6, or absence, Fig. 7, of PH-GFP). The model also allowed us to perform thought experiments (Fig. 8 and Fig. 9) that helped illuminate an important controversy in the literature on how to interpret results from this valuable and increasingly accepted live-cell assay for phosphoinositide turnover.

Materials and methods

Preparation and treatment of cells prelabeled with [³H]inositol

N1E-115 cells were grown to 30–40% confluency in 35-mm culture dishes. Approximately 4×10^5 cells per culture dish were incubated with 4 μCi/ml of myo-[2-³H]inositol (PerkinElmer) in Eagle's basal medium containing 0.5% dialyzed heat-inactivated FBS for 48 h. After two rinses to remove the unincorporated ³H radioactivity, the cells from each culture dish were scraped and suspended in 1 ml Eagle's balanced salt solution (EBSS). A 0.5-ml portion was homogenized and used for protein assay. Aliquots of 1.0 ml were transferred to 12-ml disposable screw cap polypropylene centrifuge tubes and used for each timed incubation (0, 5, 10, 20, 30, 60, 120, and 150 s) with EBSS containing 1 μM bradykinin. The incubation was terminated by pipetting 2 ml methanol to the tube. Then, 3 ml chloroform was added, followed by 1 ml 2.4 N HCl. The mixture was suspended by vortexing, and was centrifuged at 400 g for 10 min to separate the aqueous and organic phases. The lower layer was withdrawn, and the aqueous phase was reextracted with 2 ml chloroform. The two organic extracts were combined.

[³H]phosphoinositide analysis

Separation of phosphoinositides was performed as described by Kaya et al. (1989). In brief, the lipid solution was dried under N$_2$, redissolved in chloroform/methanol (7:3, vol/vol) and applied to a TLC plate (LK5D, Whatman) impregnated with 1% potassium oxalate and 2 mM EDTA, followed by development with an alkaline solvent system of chloroform, methanol, and 4 N NH$_4$OH (45:35:10, vol/vol/vol; Gonzalez-Sastre and Folch-Pi, 1968) to separate phosphoinositides. All procedures were conducted at RT. The phosphoinositides were identified by co-migration with authentic lipid standards that were visualized with phosphomolybdic acid spray reagent (Sigma-Aldrich). The silica gel area containing radioactivity was scraped, incubated with 100 μl Soluene®-350 overnight (Packard Instrument Co.), and then suspended in CytoScint ES (ICN Biomedicals) and assayed for radioactivity with a scintillation counter (model 2000 CA; Packard Instrument Co.). After treatment with Soluene®-350, recovery of the ³H radioactivity applied to the silica gel was almost 100%.

[³²P]PIP$_2$ analysis

To examine the relative PIP$_2$ content of membrane, N1E-115 cells were grown to 30–40% confluency in 35-mm culture dishes. Approximately 4×10^5 cells per culture dish were labeled to equilibrium (48 h) with 25 μCi/ml [³²P]PO$_4$ (carrier free; ICN Biomedicals) at 37°C in EBSS. After washing twice to remove the unincorporated ³²P, the cells were scraped and suspended with EBSS. Cell lipids were extracted with acidic chloroform-methanol as described previously (Agranoff et al., 1983). A 20-μl aliquot of the lipid extract was subjected to TLC using TLC plates (LK5D; Whatman) impregnated with 1% potassium oxalate and 2 mM EDTA, and the mobile phase chloroform/methanol/4 N NH$_4$OH (45:35:10; Gonzalez-Sastre and Folch-Pi, 1968). Radioactive bands were identified by co-chromatography of a PIP$_2$ standard. TLC spots were transferred to scintillation vials, suspended in CytoScint ES (ICN Biomedicals), and radioactivity was determined by liquid scintillation counting (model 2000 CA scintillation counter; Packard Instrument Co.). A second 20-μl aliquot of the lipid extract was applied to a piece of silica gel scraped from a blank TLC plate with area similar to the scraped PIP$_2$ spots, and suspended in CytoScint ES to determine radioactivity of the total lipids spotted.

Cell culture and transfections

N1E-115 neuroblastoma cells were seeded in 35-mm culture dishes at ~15,000 cells per dish on 22-mm glass coverslips, and cultured in 2.5 ml of DME supplemented with 10% FCS and antibiotics. PH-GFP constructs (Stauffer et al., 1998; a gift from Dr. Kees Jalink, The Netherlands Cancer Institute, Amsterdam, Netherlands) were transfected for 3 h using LipofectAMINE™ at 1 μg DNA/dish. After transfection, cells were incubated in DME containing 0.5% FBS and 1% DMSO for 36–48 h.

Confocal microscopy and image analysis

For confocal imaging, culture dishes with coverslips were mounted on an inverted confocal microscope (LSM 510; Carl Zeiss MicroImaging, Inc.) equipped with a 63× 1.40 oil objective (Plan-Apochromat®; Carl Zeiss MicroImaging, Inc.). Excitation of GFP was with the 488-nm argon ion laserline, and GFP fluorescence from the PH-GFP fusion protein was recorded through an emission filter (LP505; Carl Zeiss MicroImaging, Inc.). For all experiments, the pinhole size was kept the same (axial resolution of ~1.2 μM). Bradykinin was added in 20-μl aliquots to the culture dish, so that the addition (final concentration was 1 μM) was nearly instantaneous, but with as little cellular disturbance as possible. For translocation studies, a series of confocal images were taken at 5-s intervals. Direct determination of the ratio of membrane to cytosolic fluorescence by post-acquisition linescan profiles across each of the cells was confounded by the shape changes of cells during experiments (see Results). Using MetaMorph® software (Universal Imaging Corp.), a region of interest was assigned for each cell including part of the membrane, cytosol, and background. To measure the fluorescence of the membrane section inside a region of interest, a thresholding step was used to segment the membrane region, and the average fluorescence above this threshold was measured as the membrane fluorescence. The same region of interest and threshold were then applied for each image in a series. We found this approach could resolve the problem caused by cell movements and shape changes, and let us reliably detect changes in membrane fluorescence. The cytosolic fluorescence was measured by directly assigning regions of interests for cytosol.

Quantitation of cytosolic PH-GFP levels

The cytosolic PH-GFP concentration was determined in situ by using calibration slides containing known concentrations of purified, bacterially expressed PH-GFP (a gift from Dr. Laurinda Jaffe, University of Connecticut Health Center, Farmington, CT, and Dr. Tamas Balla, National Institutes of Health, Bethesda, MD). The purity of PH-GFP protein was confirmed by SDS-PAGE analysis, and the stock concentration (1 μg/μl) was measured by the BCA Protein Assay (Pierce Chemical Co.). Calibration slides were made by preparing various dilutions of the stock PH-GFP in EBSS, and imaging the fluorophore between two coverslips with the same parameters as used for the cellular PH-GFP imaging (Fink et al., 1998).

Computational modeling

The Virtual Cell software environment (available at http://www. nrcam.uchc.edu) was used to develop a model of PIP_2 turnover. The mathematical details of the model are provided in Fig. 2 and the Appendix. The model may be accessed and copied by logging in to the Virtual Cell and opening the "published" model called "PIP_2 hydrolysis." This will permit visualization of the time course and/or spatial distribution of all the variables in the model including those that were not presented in this paper. A set of instructions for downloading the model in either an XML-compliant format or as in the VCMDL format is available at http://www. nrcam.uchc.edu/applications.html.

Appendix

Model equations and parameters

The reactions labeled in red in Fig. 2 are governed by the rates as follows: Brackets, [], surround molecular species that are variables in the model. Plasma membrane species are designated by PM suffixes, and cytosolic species with Cyt suffixes.

PIPsyn: (Ratebasal_PIPsyn + Ratestim_PIPsyn) * [PI_PM]
Ratestim_PIPsyn = kStimSynPIP * exp(−((t − tauPIPsyn)/PIPsyndecay)) * (t > tauPIPsyn)
Ratebasal_PIPsyn = (kBasalSynPIP * 0.581 * (−1.0 + exp(((PIP_init − [PIP_PM])/PIP_init)))) * ([PIP_PM] < PIP_init)

PIP_2syn: (Rate_PIP_2Synbasal + Rate_PIP_2SynStim) * [PIP_PM]
Rate_PIP_2SynStim = kStimSynPIP2 * exp(−((t − tauPIP2syn)/PIP2syndecay)) * (t > tauPIP2syn)
Rate_PIP_2Synbasal = (kBasalSynPIP2 * 0.581 * (−1.0 + exp(((PIP2_basal − [PIP2_PM])/PIP2_basal)))) * ([PIP2_PM] < PIP2_basal)

PLCact: (kfPLCact * ([PLC_PM] * signal)) − (krPLCact * [PLC_act_PM])
Signal = (t > tau0) * exp(−((t − tau0)/stimdecay))

PIP_2_hyd: k_PIP_2hyd * [PIP2_PM] * [PLC_act_PM]

PIP_2_PH: (kf_PIP_2PH * [PH_GFP_Cyt] * [PIP2_PM]) − (kf_PIP_2PH * Kd_PIP_2PH * [PIP2_PHGFP_PM])

Table AI. **Parameter values for the simulation in Fig. 1**

Parameter	Value	Comments
IP_3_basal	0.16 μM	Fink et al., 1999a, 2000
IP_3_Diff	283 μm²/s	Allbritton et al., 1992
KfPLCact	5.0E-4 s⁻¹	Best fit to Fig. 1
PIP_2_basal	4,000.0 molecules/μm²	Measured
PIP_2syndecay, PIPsyndecay, stimdecay	2,857.0 molecules/μm²	Best fit to Fig. 1 and appropriate for required rate of $InsP_3$ production
PIP_basal	1.0 s	Measured
PI_PM_init	142,857.0 molecules/μm²	Measured
PLC_PM_init	100.0 molecules/μm²	Best fit to Fig. 1 (dependent on kfPLCact)
PLC_act_PM_init	0.0 molecules/μm²	Basal activity is implicit in maintenance of basal $InsP_3$ of 0.16 μM
SurfToVol_NM	1.0	Spherical nucleus of radius 3 μm
SurfToVol_PM	0.5	Calculated for a hemispherical cell of radius 9 μm; the N1E-115 neuroblastoma cells are often significantly larger, but their many processes and convoluted membrane makes this a good estimate
kBasalSynPIP	0.0055 s⁻¹	Chosen to maintain near-constant supply of PIP
kBasalSynPIP2	0.048 s⁻¹	Chosen to reproduce recovery phase of PIP_2 (Fig. 1)
kIP_3deg	0.08 s⁻¹	Based on value of 0.16 s⁻¹ at 37°C from Fink et al. (1999a)
kStimSynPIP	0.019 s⁻¹	Fit to experimental data in Fig. 1
kStimSynPIP2	0.92 s⁻¹	Fit to experimental data in Fig. 1
k_PIP2hyd	2.4 (s·molecules/μm²)⁻¹	Appropriate for required rate of $InsP_3$ production
krPLCact	0.1 s⁻¹	Appropriate for required rate of $InsP_3$ production
tau0, tauPIP2syn, tauPIPsyn	0.05 s	Stimulation introduced at 50 ms

Table AII. **Additional parameters for model of PH-GFP translocation**

Parameter	Value	Comments
KdPIP$_2$PH	2.0 μM	Hirose et al., 1999
KdIP$_3$PH	0.1 μM	Hirose et al., 1999
PH_GFP_Cyt_init	2.31 μM	Calculated from measured total PH-GFP of 6 μM, basal InsP$_3$ of 0.16 μM, and literature value of KdIP$_3$PH of 0.1 μM
IP$_3$_PHGFP_Cyt_init	3.70 μM	Calculated from measured total PH-GFP of 6 μM, basal InsP$_3$ of 0.16 μM, and literature value of KdIP$_3$PH of 0.1 μM
PHGFP_Diff	50 μm^2/s	Diffusion coefficient estimated from molecular weight
IP$_3$_PHGFP_Diff	50 μm^2/s	Diffusion coefficient estimated from molecular weight
PIP$_2$_PHGFP_PM_init	4,617.4 molecules/μm^2	Calculated from measured total PH_GFP_Cyt_init of 2.30769 μM, basal PIP$_2$ of 4,000 molecules/μm^2, and literature value of KdPIP$_2$PH of 2 μM (Hirose et al., 1999)
kf_IP$_3$PH	10.0 (μM·s)$^{-1}$	Near diffusion controlled
kf_PIP$_2$PH	0.12 (μM·s)$^{-1}$	van der Wal et al., 2001

IP$_3$_PHGFP: (kf_IP$_3$PH * [PH_GFP_Cyt] * [IP$_3$_Cyt]) − (kf_IP$_3$PH * KdIP$_3$PH * [IP$_3$_PHGFP_Cyt])

IP$_3$deg: kIP$_3$deg * ([IP$_3$_Cyt] − IP$_3$_basal)

IP$_3$_uncaging: intensity * [IP$_3$X_Cyt] * [hv_Cyt]

The rate of change of any molecular species is given by the sum of all the individual reaction rates that produce it minus all the rates that degrade it. For a spatial model, diffusion of molecules in the cytosol also has to be to be taken into account. For example, the partial differential equation governing the temporal and spatial variation of InsP$_3$ is:

$$\frac{\partial [IP3]}{\partial t} = IP3\_Diff \cdot \nabla^2 [[IP3] + PIP2\_hyd$$
$$- IP3\_PHGFP - IP3deg$$

For compartmental (i.e., nonspatial) models, diffusion is considered to be instantaneous on the time scale of interest, and the equations reduce to a set of ordinary differential equations containing just the reaction rates with appropriate adjustments for the surface-to-volume ratio of the plasma membrane to the cytosol (SurfToVol_PM). Both spatial and compartmental models for the pathways in Fig. 2 were developed in this work. The set of ordinary differential equations generated for the compartmental models were solved numerically using the LSODA stiff solver (variable time step) available within the Virtual Cell. Spatial models were solved with the finite volume method using a time step of 1 ms and a two-dimensional spatial mesh of 116 × 172 elements (x,y), each with dimensions of 0.42 × 0.42 μm. A fourfold correction for the lower surface-to-volume ratio of the two-dimensional geometry compared with the actual three-dimensional geometry of the cell was also included in the model. The model and all the simulation results may be examined by logging into the Virtual Cell at http://www.nrcam.uchc.edu; the model is named "PIP$_2$ Hydrolysis" and can be accessed by unchecking "Private only" under the "View menu." By copying the model into a new workspace, the reader may modify the model by changing parameters or adding new model components.

References

Agranoff, B.W., P. Murthy, and E.B. Seguin. 1983. Thrombin-induced phosphodiesteratic cleavage of phosphatidylinositol bisphosphate in human platelets. *J. Biol. Chem.* 258:2076–2078.

Allbritton, N.L., T. Meyer, and L. Stryer. 1992. Range of messenger action of calcium ion and inositol 1,4,5-trisphosphate. *Science.* 258:1812–1815.

Balla, T., T. Bondeva, and P. Varnai. 2000. How accurately can we image inositol lipids in living cells? *Trends Pharmacol. Sci.* 21:238–241.

Berridge, M.J. 1993. Cell signalling. A tale of two messengers. *Nature.* 365:388–389.

Berridge, M.J., and R.F. Irvine. 1984. Inositol trisphosphate, a novel second messenger in cellular signal transduction. *Nature.* 312:315–321.

Carney, D.H., D.L. Scott, E.A. Gordon, and E.F. LaBelle. 1985. Phosphoinositides in mitogenesis: neomycin inhibits thrombin-stimulated phosphoinositide turnover and initiation of cell proliferation. *Cell.* 42:479–488.

Chahwala, S.B., L.F. Fleischman, and L. Cantley. 1987. Kinetic analysis of guanosine 5′-O-(3-thiotriphosphate) effects on phosphatidylinositol turnover in NRK cell homogenates. *Biochemistry.* 26:612–622.

Ciapa, B., B. Borg, and M. Whitaker. 1992. Polyphosphoinositide metabolism during the fertilization wave in sea urchin eggs. *Development.* 115:187–195.

Coggan, J.S., and S.H. Thompson. 1995. Intracellular calcium signals in response to bradykinin in individual neuroblastoma cells. *Am. J. Physiol.* 269:C841–C848.

Coggan, J.S., and S.H. Thompson. 1997. Cholinergic modulation of the Ca^{2+} response to bradykinin in neuroblastoma cells. *Am. J. Physiol.* 273:C612–C617.

Czech, M.P. 2000. PIP2 and PIP3: complex roles at the cell surface. *Cell.* 100:603–606.

Downing, G.J., S. Kim, S. Nakanishi, K.J. Catt, and T. Balla. 1996. Characterization of a soluble adrenal phosphatidylinositol 4-kinase reveals wortmannin sensitivity of type III phosphatidylinositol kinases. *Biochemistry.* 35:3587–3594.

Ferguson, K.M., M.A. Lemmon, J. Schlessinger, and P.B. Sigler. 1995. Structure of the high affinity complex of inositol trisphosphate with a phospholipase C pleckstrin homology domain. *Cell.* 83:1037–1046.

Fink, C., F. Morgan, and L.M. Loew. 1998. Intracellular fluorescent probe concentrations by confocal microscopy. *Biophys. J.* 75:1648–1658.

Fink, C.C., B. Slepchenko, I.I. Moraru, J. Schaff, J. Watras, and L.M. Loew. 1999a. Morphological control of inositol-1,4,5-trisphosphate-dependent signals. *J. Cell Biol.* 147:929–936.

Fink, C.C., B. Slepchenko, and L.M. Loew. 1999b. Determination of time-dependent inositol-1,4,5-trisphosphate concentrations during calcium release in a smooth muscle cell. *Biophys. J.* 77:617–628.

Fink, C.C., B. Slepchenko, I.I. Moraru, J. Watras, J.C. Schaff, and L.M. Loew. 2000. An image-based model of calcium waves in differentiated neuroblastoma cells. *Biophys. J.* 79:163–183.

Gonzalez-Sastre, F., and J. Folch-Pi. 1968. Thin-layer chromatography of the phosphoinositides. *J. Lipid Res.* 9:532–533.

Halet, G., R. Tunwell, T. Balla, K. Swann, and J. Carroll. 2002. The dynamics of

plasma membrane PtdIns(4,5)P(2) at fertilization of mouse eggs. *J. Cell Sci.* 115:2139–2149.

Higashida, H., and D.A. Brown. 1987. Bradykinin inhibits potassium (M) currents in N1E-115 neuroblastoma cells. Responses resemble those in NG108-15 neuroblastoma x glioma hybrid cells. *FEBS Lett.* 220:302–306.

Hilgemann, D.W., S. Feng, and C. Nasuhoglu. 2001. The complex and intriguing lives of PIP2 with ion channels and transporters. *Sci. STKE.* 2001:RE19.

Hirose, K., S. Kadowaki, M. Tanabe, H. Takeshima, and M. Iino. 1999. Spatiotemporal dynamics of inositol 1,4,5-trisphosphate that underlies complex Ca^{2+} mobilization patterns. *Science.* 284:1527–1530.

Holz, R.W., M.D. Hlubek, S.D. Sorensen, S.K. Fisher, T. Balla, S. Ozaki, G.D. Prestwich, E.L. Stuenkel, and M.A. Bittner. 2000. A pleckstrin homology domain specific for phosphatidylinositol 4,5-bisphosphate (PtdIns-4,5-P2) and fused to green fluorescent protein identifies plasma membrane PtdIns-4,5-P2 as being important in exocytosis. *J. Biol. Chem.* 275:17878–17885.

Huijbregts, R.P., L. Topalof, and V.A. Bankaitis. 2000. Lipid metabolism and regulation of membrane trafficking. *Traffic.* 1:195–202.

Jain, M.K. 1980. Membrane components: isolation, composition, and metabolism. *In* Introduction to Biological Membranes. M.K. Jain and R.C. Wagner, editors. John Wiley and Sons, Inc., New York. 25–52.

Kaya, H., G.M. Patton, and S.L. Hong. 1989. Bradykinin-induced activation of phospholipase A2 is independent of the activation of polyphosphoinositide-hydrolyzing phospholipase C. *J. Biol. Chem.* 264:4972–4977.

Kavran, J.M., D.E. Klein, A. Lee, M. Falasca, S.J. Isakoff, E.Y. Skolnik, and M.A. Lemmon. 1998. Specificity and promiscuity in phosphoinositide binding by pleckstrin homology domains. *J. Biol. Chem.* 273:30497–30508.

Kiss, Z., and T. Farkas. 1975. The effect of isoproterenol on the metabolism of phosphatidylinositol by rat heart in vitro. *Biochem. Pharmacol.* 24:999–1002.

Lange, Y., M.H. Swaisgood, B.V. Ramos, and T.L. Steck. 1989. Plasma membranes contain half the phospholipid and 90% of the cholesterol and sphingomyelin in cultured human fibroblasts. *J. Biol. Chem.* 264:3786–3793.

Lassing, I., and U. Lindberg. 1990. Polyphosphoinositide synthesis in platelets stimulated with low concentrations of thrombin is enhanced before the activation of phospholipase C. *FEBS Lett.* 262:231–233.

Lemmon, M.A., K.M. Ferguson, R. O'Brien, P.B. Sigler, and J. Schlessinger. 1995. Specific and high-affinity binding of inositol phosphates to an isolated pleckstrin homology domain. *Proc. Natl. Acad. Sci. USA.* 92:10472–10476.

Loew, L.M., and J.C. Schaff. 2001. The Virtual Cell: A software environment for computational cell biology. *Trends Biotechnol.* 19:401–406.

Lukacova, N., and J. Marsala. 1997. Regional distribution of phospholipids and polyphosphatidyl inositides in the rabbit's spinal cord. *Neurochem. Res.* 22:687–692.

Manifava, M., J.W. Thuring, Z.Y. Lim, L. Packman, A.B. Holmes, and N.T. Ktistakis. 2001. Differential binding of traffic-related proteins to phosphatidic acid- or phosphatidylinositol (4,5)-bisphosphate-coupled affinity reagents. *J. Biol. Chem.* 276:8987–8994.

Martin, T.F. 2001. PI(4,5)P(2) regulation of surface membrane traffic. *Curr. Opin. Cell Biol.* 13:493–499.

McLaughlin, S., N. Mulrine, T. Gresalfi, G. Vaio, and A. McLaughlin. 1981. Adsorption of divalent cations to bilayer membranes containing phosphatidylserine. *J. Gen. Physiol.* 77:445–473.

McLaughlin, S., J. Wang, A. Gambhir, and D. Murray. 2002. PIP(2) and proteins: interactions, organization, and information flow. *Annu. Rev. Biophys. Biomol. Struct.* 31:151–175.

Mitchell, C.A., S. Brown, J.K. Campbell, A.D. Munday, and C.J. Speed. 1996. Regulation of second messengers by the inositol polyphosphate 5-phosphatases. *Biochem. Soc. Trans.* 24:994–1000.

Mitchell, R.H., C.J. Kirk, L.M. Jones, C.P. Downes, and J.A. Creba. 1981. The stimulation of inositol lipid metabolism that accompanies calcium mobilization in stimulated cells: defined characteristics and unanswered questions. *Philos. Trans. R. Soc. Lond. B Biol. Sci.* 296:123–138.

Nakanishi, S., K.J. Catt, and T. Balla. 1995. A wortmannin-sensitive phosphatidylinositol 4-kinase that regulates hormone-sensitive pools of inositolphospholipids. *Proc. Natl. Acad. Sci. USA.* 92:5317–5321.

Nash, M.S., K.W. Young, G.B. Willars, R.A. Challiss, and S.R. Nahorski. 2001. Single-cell imaging of graded Ins(1,4,5)P3 production following G-protein-coupled-receptor activation. *Biochem. J.* 356:137–142.

Nebl, T., S.W. Oh, and E.J. Luna. 2000. Membrane cytoskeleton: PIP(2) pulls the strings. *Curr. Biol.* 10:R351–R354.

Nemoto, Y., M. Arribas, C. Haffner, and P. DeCamilli. 1997. Synaptojanin 2, a novel synaptojanin isoform with a distinct targeting domain and expression pattern. *J. Biol. Chem.* 272:30817–30821.

Okubo, Y., S. Kakizawa, K. Hirose, and M. Iino. 2001. Visualization of InsP(3) dynamics reveals a novel AMPA receptor-triggered InsP(3) production pathway mediated by voltage-dependent Ca(2+) influx in Purkinje cells. *Neuron.* 32:113–122.

Quist, E.E. 1982. Evidence for a carbachol stimulated phosphatidylinositol effect in heart. *Biochem. Pharmacol.* 31:3130–3133.

Quist, E., and M. Sanchez. 1983. Alpha adrenergic drugs induce a phospholipid effect in canine heart. *Proc. West. Pharmacol. Soc.* 26:333–335.

Payrastre, B., K. Missy, S. Giuriato, S. Bodin, M. Plantavid, and M. Gratacap. 2001. Phosphoinositides: key players in cell signalling, in time and space. *Cell. Signal.* 13:377–387.

Racagni, G., M. Garcia de Lema, C.E. Domenech, and E.E. Machado de Domenech. 1992. Phospholipids in *Trypanosoma cruzi*: phosphoinositide composition and turnover. *Lipids.* 27:275–278.

Rameh, L.E., K.F. Tolias, B.C. Duckworth, and L.C. Cantley. 1997. A new pathway for synthesis of phosphatidylinositol-4,5-bisphosphate. *Nature.* 390:192–196.

Rebecchi, M., A. Peterson, and S. McLaughlin. 1992. Phosphoinositide-specific phospholipase C-delta 1 binds with high affinity to phospholipid vesicles containing phosphatidylinositol 4,5-bisphosphate. *Biochemistry.* 31:12742–12747.

Rozelle, A.L., L.M. Machesky, M. Yamamoto, M.H. Driessens, R.H. Insall, M.G. Roth, K. Luby-Phelps, G. Marriott, A. Hall, and H.L. Yin. 2000. Phosphatidylinositol 4,5-bisphosphate induces actin-based movement of raft-enriched vesicles through WASP-Arp2/3. *Curr. Biol.* 10:311–320.

Sakisaka, T., T. Itoh, K. Miura, and T. Takenawa. 1997. Phosphatidylinositol 4,5-bisphosphate phosphatase regulates the rearrangement of actin filaments. *Mol. Cell. Biol.* 17:3841–3849.

Schaff, J., C.C. Fink, B. Slepchenko, J.H. Carson, and L.M. Loew. 1997. A general computational framework for modeling cellular structure and function. *Biophys. J.* 73:1135–1146.

Schaff, J.C., B.M. Slepchenko, Y. Choi, J.M. Wagner, D. Resasco, and L.M. Loew. 2001. Analysis of non-linear dynamics on arbitrary geometries with the Virtual Cell. *Chaos.* 11:115–131.

Sechi, A.S., and J. Wehland. 2000. The actin cytoskeleton and plasma membrane connection: PtdIns(4,5)P(2) influences cytoskeletal protein activity at the plasma membrane. *J. Cell Sci.* 113:3685–3695.

Sekar, M.C., and B.D. Roufogalis. 1984. Comparison of muscarinic and alpha-adrenergic receptors in rat atria based on phosphoinositide turnover. *Life Sci.* 35:1527–1533.

Slepchenko, B.M., J.C. Schaff, J.H. Carson, and L.M. Loew. 2002. Computational cell biology: spatiotemporal simulation of cellular events. *Annu. Rev. Biophys. Biomol. Struct.* 31:423–441.

Snow, P., D.L. Yim, J.D. Leibow, S. Saini, and R. Nuccitelli. 1996. Fertilization stimulates an increase in inositol trisphosphate and inositol lipid levels in Xenopus eggs. *Dev. Biol.* 180:108–118.

Stauffer, T.P., S. Ahn, and T. Meyer. 1998. Receptor-induced transient reduction in plasma membrane PtdIns(4,5)P2 concentration monitored in living cells. *Curr. Biol.* 8:343–346.

Stefan, C.J., A. Audhya, and S.D. Emr. 2002. The yeast synaptojanin-like proteins control the cellular distribution of phosphatidylinositol (4,5)-bisphosphate. *Mol. Biol. Cell.* 13:542–557.

Stith, B.J., M. Goalstone, S. Silva, and C. Jaynes. 1993. Inositol 1,4,5-trisphosphate mass changes from fertilization through first cleavage in *Xenopus laevis*. *Mol. Biol. Cell.* 4:435–443.

Stith, B.J., R. Espinoza, D. Roberts, and T. Smart. 1994. Sperm increase inositol 1,4,5-trisphosphate mass in *Xenopus laevis* eggs preinjected with calcium buffers or heparin. *Dev. Biol.* 165:206–215.

Suh, B.C., and B. Hille. 2002. Recovery from muscarinic modulation of M current channels requires phosphatidylinositol 4,5-bisphosphate synthesis. *Neuron.* 35:507–520.

Takenawa, T., T. Itoh, and K. Fukami. 1999. Regulation of phosphatidylinositol 4,5-bisphosphate levels and its roles in cytoskeletal re-organization and malignant transformation. *Chem. Phys. Lipids.* 98:13–22.

Tolias, K.F., and L.C. Cantley. 1999. Pathways for phosphoinositide synthesis. *Chem. Phys. Lipids.* 98:69–77.

Toker, A. 1998. The synthesis and cellular roles of phosphatidylinositol 4,5-bisphosphate. *Curr. Opin. Cell Biol.* 10:254–261.

Turner, P.R., M.P. Sheetz, and L.A. Jaffe. 1984. Fertilization increases the polyphosphoinositide content of sea urchin eggs. *Nature.* 310:414–415.

van der Wal, J., R. Habets, P. Varnai, T. Balla, and K. Jalink. 2001. Monitoring agonist-induced phospholipase C activation in live cells by fluorescence resonance energy transfer. *J. Biol. Chem.* 276:15337–15344.

van Rheenen, J., and K. Jalink. 2002. Agonist-induced PIP(2) hydrolysis inhibits cortical actin dynamics: regulation at a global but not at a micrometer scale. *Mol. Biol. Cell.* 13:3257–3267.

Vanhaesebroeck, B., S.J. Leevers, K. Ahmadi, J. Timms, R. Katso, P.C. Driscoll, R. Woscholski, P.J. Parker, and M.D. Waterfield. 2001. Synthesis and function of 3-phosphorylated inositol lipids. *Annu. Rev. Biochem.* 70:535–602.

Varnai, P., and T. Balla. 1998. Visualization of phosphoinositides that bind pleckstrin homology domains: calcium- and agonist-induced dynamic changes and relationship to myo-[³H]inositol-labeled phosphoinositide pools. *J. Cell Biol.* 143:501–510.

Varnai, P., X. Lin, S.B. Lee, G. Tuymetova, T. Bondeva, A. Spat, S.G. Rhee, G. Hajnoczky, and T. Balla. 2002. Inositol lipid binding and membrane localization of isolated pleckstrin homology (PH) domains. Studies on the PH domains of phospholipase C delta 1 and p130. *J. Biol. Chem.* 277:27412–27422.

Warnock, D.E., C. Roberts, M.S. Lutz, W.A. Blackburn, W.W. Young, Jr., and J.U. Baenziger. 1993. Determination of plasma membrane lipid mass and composition in cultured Chinese hamster ovary cells using high gradient magnetic affinity chromatography. *J. Biol. Chem.* 268:10145–10153.

Watt, S.A., G. Kular, I.N. Fleming, C.P. Downes, and J.M. Lucocq. 2002. Subcellular localization of phosphatidylinositol 4,5-bisphosphate using the pleckstrin homology domain of phospholipase C delta1. *Biochem. J.* 363:657–666.

Willars, G.B., S.R. Nahorski, and R.A.J. Challiss. 1998. Differential regulation of muscarinic acetylcholine receptor-sensitive polyphosphoinositide pools and consequences for signaling in human neuroblastoma cells. *J. Biol. Chem.* 273:5037–5046.

Xu, C., and L.M. Loew. 2003. Activation of phospholipase C increases intramembrane electric fields in N1E-115 neuroblastoma cells. *Biophys. J.* In press.

Yorek, M.A., J.A. Dunlap, M.R. Stefani, E.P. Davidson, X. Zhu, and J. Eichberg. 1994. Decreased myo-inositol uptake is associated with reduced bradykinin-stimulated phosphatidylinositol synthesis and diacylglycerol content in cultured neuroblastoma cells exposed to L-fucose. *J. Neurochem.* 62:147–158.

Zhang, H., L.C. Craciun, T. Mirshahi, T. Rohacs, C.M. Lopes, T. Jin, and D.E. Logothetis. 2003. PIP(2) activates KCNQ channels, and its hydrolysis underlies receptor-mediated inhibition of M currents. *Neuron.* 37:963–975.